Energy &
Environmental
Science

ROYAL SOCIETY
OF CHEMISTRY

PAPER

View Article Online
View Journal | View Issue

Check for updates

Cite this: *Energy Environ. Sci.*, 2021, **14**, 1469

$Na_2Fe_2F_7$: a fluoride-based cathode for high power and long life Na-ion batteries†

Hyunyoung Park, ‡[ab] Yongseok Lee, ‡[ab] Min-kyung Cho,[c] Jungmin Kang,[ab] Wonseok Ko,[ab] Young Hwa Jung,[d] Tae-Yeol Jeon,[d] Jihyun Hong,[e] Hyungsub Kim,[f] Seung-Taek Myung *[a] and Jongsoon Kim *[ab]

Received 1st September 2020,
Accepted 25th November 2020

DOI: 10.1039/d0ee02803g

rsc.li/ees

Despite the high energy density of layered-type cathode materials for Na-ion batteries, their two-dimensional crystal structure suffers a large volume change and phase transition during Na^+ de/intercalation, which often results in their poor cycling performances. Thus, a robust three-dimensional framework with minimal structural change is required for stable electrochemical sodium storage. Here, we introduce an earth-abundant element-based trigonal-type Na–Fe–F compound ($Na_2Fe_2F_7$) with three-dimensionally interconnected FeF_6 octahedra and three-dimensional Na^+ diffusion pathways. Through combined studies using first-principles calculations and experiments, we confirm that $Na_2Fe_2F_7$ delivers excellent power-capability due to large three-dimensional Na^+ diffusion pathways as well as ultra-long cycling performance due to negligible structural change during Na^+ de/intercalation. These results will guide new insights for material discovery for high performance rechargeable batteries.

Broader context

We report the trigonal-type $Na_2Fe_2F_7$ (T-$Na_2Fe_2F_7$) cathode material with a three-dimensional framework for Na-ion batteries (NIBs). Generally, the layered-type cathode materials, such as Na_xMO_2, are considered as a promising cathode for NIBs because of their large gravimetric capacity and facile Na^+ diffusion; however, they exhibit poor cycling performances due to large volume change and phase transition during Na^+ de/intercalation. Meanwhile, T-$Na_2Fe_2F_7$ which consists of three-dimensionally interconnected FeF_6 octahedra with high structural stability has large three-dimensional Na^+ diffusion pathways indicating the feasibility of facile Na^+ diffusion resulting in outstanding electrochemical performances. Through first-principles calculations, the theoretical capacity of T-$Na_2Fe_2F_7$ was predicted as $\sim$184 mA h g^{-1} *via* the Fe^{2+}/Fe^{3+} redox reaction with an average operation voltage of $\sim$3.1 V (*vs.* Na^+/Na) corresponding to 2 mol of Na storage per formula unit of $Na_2Fe_2F_7$. T-$Na_2Fe_2F_7$ reached the capacity of $\sim$184 mA h g^{-1} at C/20 (1C = 184 mA g^{-1}), and the specific capacity was retained at up to $\sim$88% over 1000 cycles at 2C compared to the initial capacity. The excellent power-capability and ultra-long cycling performance were based on large three-dimensional Na^+ diffusion pathways by preventing structural change. We believe that our work for T-$Na_2Fe_2F_7$ will provide insights into high performance rechargeable batteries.

Introduction

Renewable and sustainable energy sources must be considered to reduce the environmental impacts of global warming. Lithium-ion batteries (LIBs) have been predominantly adopted in not only portable devices but also large-scale energy storage systems (ESSs) because of their high capacity, long lifetime, and remarkable power-capability.[1–4] However, this system is dependent on the use of expensive Co and Ni in $LiCoO_2$ and $Li[Ni_{1-x-y}Co_xA_y]O_2$ (A: Mn or Al), which are currently used as cathode materials for commercial LIBs.[5] Many efforts to introduce economical elements such as Mn and Fe into LIBs have been made; however, the disproportionation of Mn^{3+} and the electrochemical inactivity of the Fe^{3+}/Fe^{4+} redox have hindered the use of earth-abundant elements in LIBs.

Sodium-ion batteries (NIBs) are considered promising alternatives to LIBs owing to the use of earth-abundant sodium as

---

[a] *Department of Nanotechnology and Advanced Materials Engineering, Sejong University, Seoul, 05006, Republic of Korea. E-mail: smyung@sejong.ac.kr, jongsoonkim@sejong.ac.kr*
[b] *Department of Energy Science, Sungkyunkwan University, Suwon, 16419, Republic of Korea. E-mail: jongsoonkim@skku.edu*
[c] *Advanced Analysis Center, Korea Institute of Science and Technology (KIST), Seoul, 02792, Republic of Korea*
[d] *Beamline Division, Pohang Accelerator Laboratory (PAL), Pohang, 37673, Republic of Korea*
[e] *Center for Energy Materials Research, Korea Institute of Science and Technology (KIST), Seoul, 02792, Republic of Korea*
[f] *Korea Atomic Energy Research Institute (KAERI), Daedeok-daero 989 Beon-Gil, Yuseong-gu, Daejeon, 34057, Republic of Korea*

† Electronic supplementary information (ESI) available. See DOI: 10.1039/d0ee02803g

‡ These authors contributed equally to this manuscript.

the charge carrier and the similar reaction mechanism to that of LIBs. Potential cathode materials for NIBs include layered-type sodium metal oxides (Na_xMO_2),[6–9] polyanionic compounds,[9–11] Prussian blue compounds,[12,13] and organic-based compounds.[14,15] Layered Na_xMO_2 cathode materials have attracted great interest because their large gravimetric capacity and facile Na^+ diffusion lead to outstanding power-capability. In particular, numerous Fe- and Mn-based Na_xMO_2 have been reported as promising cathodes for NIBs, because of the expected low prodcution cost by the usage of abundant Fe and Mn elements on the Earth.[16,17] Many efforts have been made to introduce Fe into a layered-type cathode for NIBs. α-$NaFeO_2$ was first discovered to be capable of chemical Na^+ deintercalation accompanying Fe^{3+}/Fe^{4+} redox reaction.[18] It was reported that O3-type $NaFeO_2$ delivers the specific capacity of 112 mA h g^{-1} with an average voltage of $\sim$3.3 V (*vs.* Na^+/Na).[19] With deintercalation of more than 0.5 mol Na^+ ions at O3-type $NaFeO_2$ when charged to 4.5 V (*vs.* Na^+/Na), however, the crystal structure is irreversibly changed by migration of iron ions. And then, the $Na_{1-x}FeO_2$ becomes a nearly inactive cathode for NIBs. For Mn-based layered cathode materials,[20] large capacities over 180 mA h g^{-1} have frequently been achieved in the initial cycles; however, they lack cycling stability because of Jahn–Teller distortion by Mn^{3+} ions and phase transitions such as P2–OP4 or O3–P3 transitions accompanied by large variations along the *c*-axis during Na^+ de/intercalation.

The combination of Fe and Mn with polyanion-connecting elements in compounds such as $Na(Fe_{1-x}Mn_x)PO_4$,[21] $Na_2(Fe_{1-x}Mn_x)PO_4F$,[22] $Na(Fe_{1-x}Mn_x)SO_4F$,[23] and $Na_2(Fe_{1-x}Mn_x)_2(SO_4)_3$[24] has resulted in electrode materials that possess excellent long-term cyclability, with the stronger bonds of P–O and S–O stabilizing the crystal structure from dramatic variation of the *c*-axis of the unit cell. However, these P–O- and S–O-based connecting elements are also the main factor reducing the gravimetric capacity relative to that of oxide materials, with the achievement of gravimetric capacities >130 mA h g^{-1} hindered by the small theoretical capacity associated with these polyanions. To simultaneously achieve the high gravimetric energy density of layered Na_xMO_2 and the high structural stability of polyanions, we focused on fluoride-based compounds ($Na_xM_yF_z$) because of the smaller molar weight of fluorine relative to that of polyanions such as phosphate (PO_4) or sulfate (SO_4) and the high operation voltage resulting from the high electronegativity of fluorine. Furthermore, most $Na_xM_yF_z$ compounds such as perovskite-type Na_xMF_3 and Na_3MF_6 possess a three-dimensionally connected framework, which implies their high structural stability in the Na-deficient phase relative to layered Na_xMO_2. However, despite the various merits resulting from the fluoride-based structure, these compounds delivered relatively poor electrochemical performance compared with that of layered Na_xMO_2 and polyanions.

In the current study, we explored the trigonal-type $Na_2Fe_2F_7$ (T-$Na_2Fe_2F_7$) structure based on three-dimensionally connected FeF_6 octahedra, which exhibits a large theoretical capacity as well as a high operation voltage derived from the inductive effect by the fluorine-based crystal structure. We confirmed the three-dimensional Na^+ diffusion pathways in the structure through Rietveld refinement and bond-valence energy landscape (BVEL) analyses based on X-ray diffraction (XRD). Using first-principles calculations, the resulting theoretical capacity was predicted to reach 184 mA h g^{-1} assisted by the Fe^{2+}/Fe^{3+} redox reaction with an average operation voltage of $\sim$3.1 V (*vs.* Na^+/Na) when 2 mol of Na^+ was available for de/intercalation in the formula unit; this capacity is the highest ever reported among three-dimensionally arranged compounds. A high capacity of 184 mA h g^{-1} was delivered at C/20 (1C = 184 mA g^{-1}), approaching the theoretical limit, associated with a single-phase reaction without any phase transition and negligible volume change below $\sim$1% during Na^+ de/intercalation by the crystal structure composed of point-shared FeF_6 octahedra. This structural feature resulted in sustainability of the structure over 1000 cycles at 2C, with over 88% of the initial capacity retained. Moreover, the specific capacity was retained at up to $\sim$70% of the theoretical capacity even at 5C, indicating outstanding power-capability of T-$Na_2Fe_2F_7$ resulting from three-dimensional Na^+ diffusion pathways. In terms of the capacity, cyclability, power-capability and operation voltage, the present trigonal $Na_2Fe_2F_7$ is comparable to layered cathode materials for NIBs, and the concept of using earth-abundant elements is suitable for cutting-edge applications for NIBs.

Results and discussion

Merits of T-$Na_2Fe_2F_7$ structures

In Fig. 1a, the crystal structure of T-$Na_2M_2F_7$ (M = transition metal) based on the structural information of T-$Na_2Fe_2F_7$ is presented and compared with that of layered-type sodium transition metal oxides (Na_xMO_2). Notably, T-$Na_2M_2F_7$ is composed of conjugated Na/M layers, which differs from the clearly separated M and Na layers in the Na_xMO_2 structure. Unlike in Na_xMO_2, where Na^+ ion diffusion is only possible *via* two-dimensional pathways, the three-dimensionally connected FeF_6 octahedra in T-$Na_2M_2F_7$ enable the creation of large three-dimensional Na^+ diffusion pathways (Fig. 1b). In particular, the presence of the three-dimensionally connected framework implies the high structural stability of the electrode materials during charge/discharge, as confirmed in previous studies on polyanion-based electrode materials.[25–28] Na_xMO_2 has been reported to undergo large elongation/shrinkage of the lattice parameters in addition to phase transition during charge/discharge because of the strengthening of the structural instability by O^{2-}–O^{2-} repulsion during Na^+ deintercalation. Thus, we expected that the three-dimensionally connected FeF_6 octahedra could suppress the large structural change of T-$Na_2M_2F_7$ during Na^+ de/intercalation, resulting in superior cycling performance and making T-$Na_2M_2F_7$ a promising cathode for NIBs compared with Na_xMO_2 compounds.

T-$Na_2Fe_2F_7$ was synthesized using a simple conventional solid-state method. Field-emission transmission electron microscopy (FE-TEM) combined with energy-dispersive X-ray spectroscopy (EDS) revealed that Na, Fe, and F elements were homogenously distributed in the T-$Na_2Fe_2F_7$ particles (Fig. S1, ESI†). In addition, the atomic ratio of Na : Fe was confirmed to be

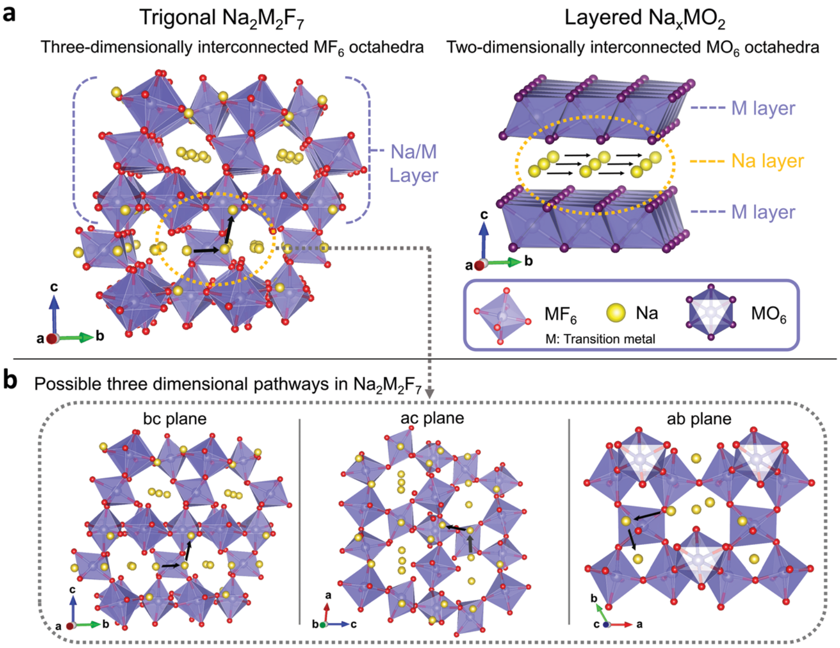

Fig. 1 (a) Schematic illustrations of the crystal structures of $Na_2M_2F_7$ and Na_xMO_2 (M = transition metal). Note that the three-dimensional framework of $Na_2M_2F_7$ enables the three-dimensional diffusion of Na^+ ions, whereas the two-dimensional framework of Na_xMO_2 only allows the migration of Na^+ ions through the Na layer. (b) Various ion diffusion pathways of a $Na_2M_2F_7$ crystal structure. A magnified view of each Na^+ migration pathway is presented, with the black arrows indicating a possible diffusion pathway of Na^+ ions.

1.99 : 2 for the T-$Na_2Fe_2F_7$ compound through inductively coupled plasma-atomic emission spectroscopy (ICP-OES) (Table S1, ESI†). Further observation of the surface morphology was performed using scanning electron microscope (SEM), and the particle shape was consistent with the FE-TEM measurements (Fig. S2, ESI†). Additionally, X-ray absorption nearest edge spectroscopy (XANES) analysis confirmed that the average oxidation state of Fe was close to $Fe^{2.5+}$ in T-$Na_2Fe_2F_7$ (Fig. S3, ESI†). This result implies that the Fe^{2+}/Fe^{3+} redox reaction can be used to reach between T-$Na_1Fe^{3+}{}_2F_7$ on charge (oxidation) and T-$Na_3Fe^{2+}{}_2F_7$ on discharge (reduction). The resulting crystal structure was determined through Rietveld refinement of XRD data (Fig. 2a). T-$Na_2Fe_2F_7$ was stabilized in a trigonal structure with $P3_121$ space group, and the corresponding lattice parameters were calculated to be $a = b = 7.3774(3)$ Å, $c = 18.2288(12)$ Å with high reliability ($R_P = 2.67\%$, $R_I = 1.61\%$, $R_F = 1.26\%$, and $\chi^2 = 1.10\%$). The presence of three Na atomic sites in T-$Na_2Fe_2F_7$ was confirmed, namely (i) Na1:6*c* (0.523, 0.849, 0.6653), (ii) Na2:6*c* (0.949, 0.186, 0.3357), and (iii) Na3:6*c* (0.902, 0.169, 0.8626). Table S2 (ESI†) presents detailed structural information for T-$Na_2Fe_2F_7$, including the atomic occupancy, thermal factor (B_{iso}), and occupancies. Interestingly, half of the Na2 and Na3 sites in the T-$Na_2Fe_2F_7$ structure are filled with sodium ions, whereas the Na1 site remains a fully occupied state. This finding implies that 1 mol of Na ions can be additionally intercalated into the Na2 and Na3 sites of the T-$Na_2Fe_2F_7$ structure to form T-$Na_3Fe_2F_7$.

Based on the above structural information for T-$Na_2Fe_2F_7$, BVEL analysis was performed using the *Bond_Str* program in the FullProf package[29] to predict the possible Na^+ positions and diffusion pathways in the structure (Fig. 2b and c). In the T-$Na_xFe_2F_7$ ($1 \leq x \leq 3$) crystal structure, all the FeF_6 octahedra are infinitely connected with each other, and there are large three-dimensional diffusion pathways, indicating the feasibility of facile Na^+ diffusion. The crystal structure of T-$Na_2Fe_2F_7$ was also confirmed through high-resolution transmission electron microscopy (HR-TEM) analyses. Fig. S4 (ESI†) shows the *d*-spacing corresponding to the (011) plane of T-$Na_2Fe_2F_7$ ($d_{(011)}$: ~6.02 Å). Selected area electron diffraction (SAED) patterns along the $[\bar{2}\bar{1}1]$ zone-axis also confirmed the trigonal-based single-crystalline structure of T-$Na_2Fe_2F_7$. In addition, it has been reported that various sodiated compounds readily absorb water molecules in air.[30,31] The as-synthesized T-$Na_2Fe_2F_7$ was exposed to air for 10 days, and no critical differences in the XRD patterns or thermogravimetric curves were observed (Fig. S5 and S6, ESI†), confirming the water stability of T-$Na_2Fe_2F_7$ in air relative to other air-sensitive layered cathode materials.[32,33]

Electrochemistry of T-$Na_2Fe_2F_7$ in NIB systems

First-principles calculations were performed for T-$Na_xFe_2F_7$ ($0.5 \leq x \leq 3$) in the Na-cell system based on the structural information from the Rietveld refinement and BVEL analyses. Fig. 3a presents the predicted theoretical redox potentials of the various T-$Na_xFe_2F_7$ compositions ($0.5 \leq x \leq 3$). For accurate prediction of the redox potentials, numerous Na^+/vacancy configurations for the T-$Na_xFe_2F_7$ compositions were generated using cluster-assisted statistical mechanics (CASM) software,[34]

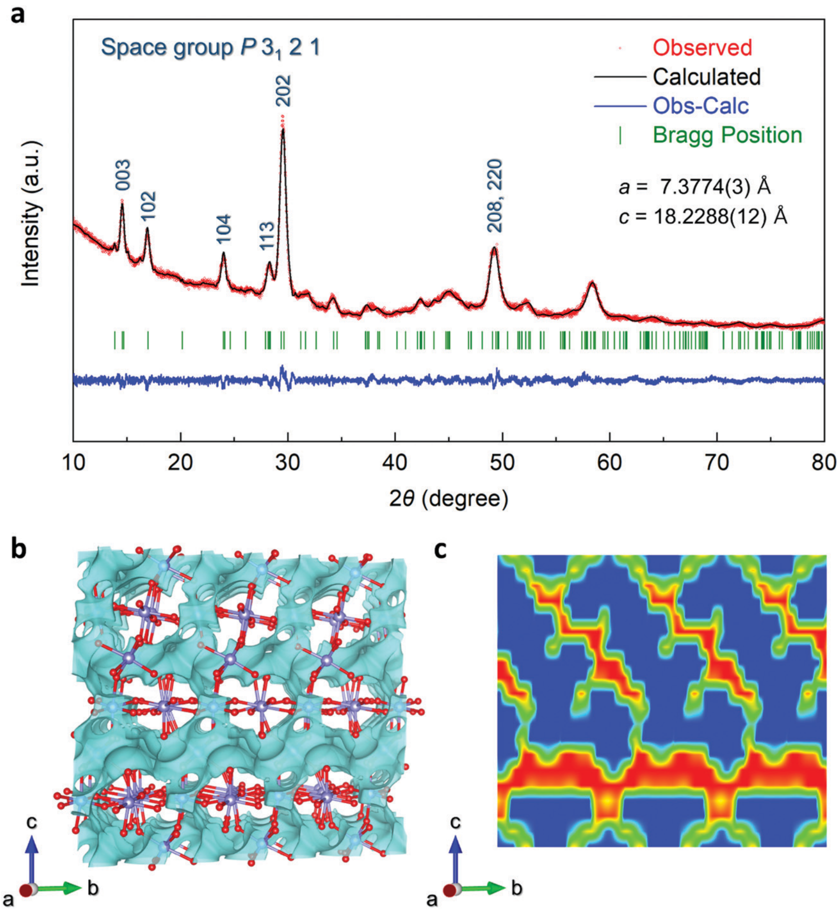

Fig. 2 (a) Rietveld refinement of the XRD pattern of T-$Na_2Fe_2F_7$. (b) Three-dimensional and (c) two-dimensional bond-valence sum energy map of T-$Na_2Fe_2F_7$ with all possible Na^+ diffusion pathways in the crystal structure.

and the resulting theoretical redox potential of T-$Na_xFe_2F_7$ was calculated using the following equation:

$$V = -\frac{E[\mathrm{Na}_{x_2}\mathrm{Fe}_2\mathrm{F}_7] - E[\mathrm{Na}_{x_1}\mathrm{Fe}_2\mathrm{F}_7] - (x_2 - x_1)E(\mathrm{Na})}{(x_2 - x_1)F}$$

Here, V is the average redox potential of T-$Na_xFe_2F_7$ in the compositional range of $x_1 \leq x \leq x_2$, and $E[\mathrm{Na}_x\mathrm{Fe}_2\mathrm{F}_7]$ is the formation energy of the most stable configuration of T-$Na_xFe_2F_7$ calculated using first-principles calculations. It was predicted that a total of 2 mol Na^+ can be reversibly de/intercalated between T-$Na_3Fe_2F_7$ and T-$Na_1Fe_2F_7$ in the available voltage range (*vs.* Na^+/Na). In addition, there are several stable intermediate phases between the T-$Na_3Fe_2F_7$ and T-$Na_1Fe_2F_7$ phases, which indicates that T-$Na_xFe_2F_7$ undergoes a single-phase reaction with monotonously sloped charge/discharge profiles during Na^+ de/intercalation. Fig. 3b shows that these theoretical results based on first-principles calculations were in good agreement with the experimentally measured galvanostatic intermittent titration technique (GITT) profile of T-$Na_xFe_2F_7$. In a GITT test, a current density of C/20 was applied for 30 min to measure the closed-circuit voltage (CCV), and it was turned off for 10 min to obtain the quasi-open-circuit voltage (QOCV). This comparison indicated a large specific capacity of 184 mA h g^{-1}, which is the theoretical capacity, corresponding to 2 mol Na^+ de/intercalation per formula unit. In particular, despite the Fe^{2+}/Fe^{3+} redox reaction, T-$Na_xFe_2F_7$ had a high average operation voltage of ∼3.1 V (*vs.* Na^+/Na) with low polarization. Most likely because of the higher electronegativity of fluorine ions than oxygen ions, electron transfer from transition-metal elements in T-$Na_xFe_2F_7$ requires more energy than that in the oxide matrix under the same conditions. Therefore, it is reasonable to consider that the present fluoride-based material brings about a higher operation voltage than oxide-based electrodes. This is similar to the increased operation voltage observed in Fe^{2+}/Fe^{3+} by the inductive effect of P with high electronegativity in $LiFePO_4$.[35] These first-principles calculation results imply that T-$Na_xFe_2F_7$ can deliver excellent energy density comparable to that of other layered-type cathode materials for NIBs.

The electrochemical tests were performed at various discharge current rates and fixed charge current rate of C/20 (1C = 184 mA g^{-1}), in the voltage range of 1.5–4.3 V. Note that in addition to delivering a large specific capacity of 184 mA h g^{-1} with an average operation voltage of ∼3.1 V (*vs.* Na^+/Na), T-$Na_xFe_2F_7$ also exhibited outstanding power-capability as a cathode for NIBs (Fig. 3c and d). Notably, even at 5C, the

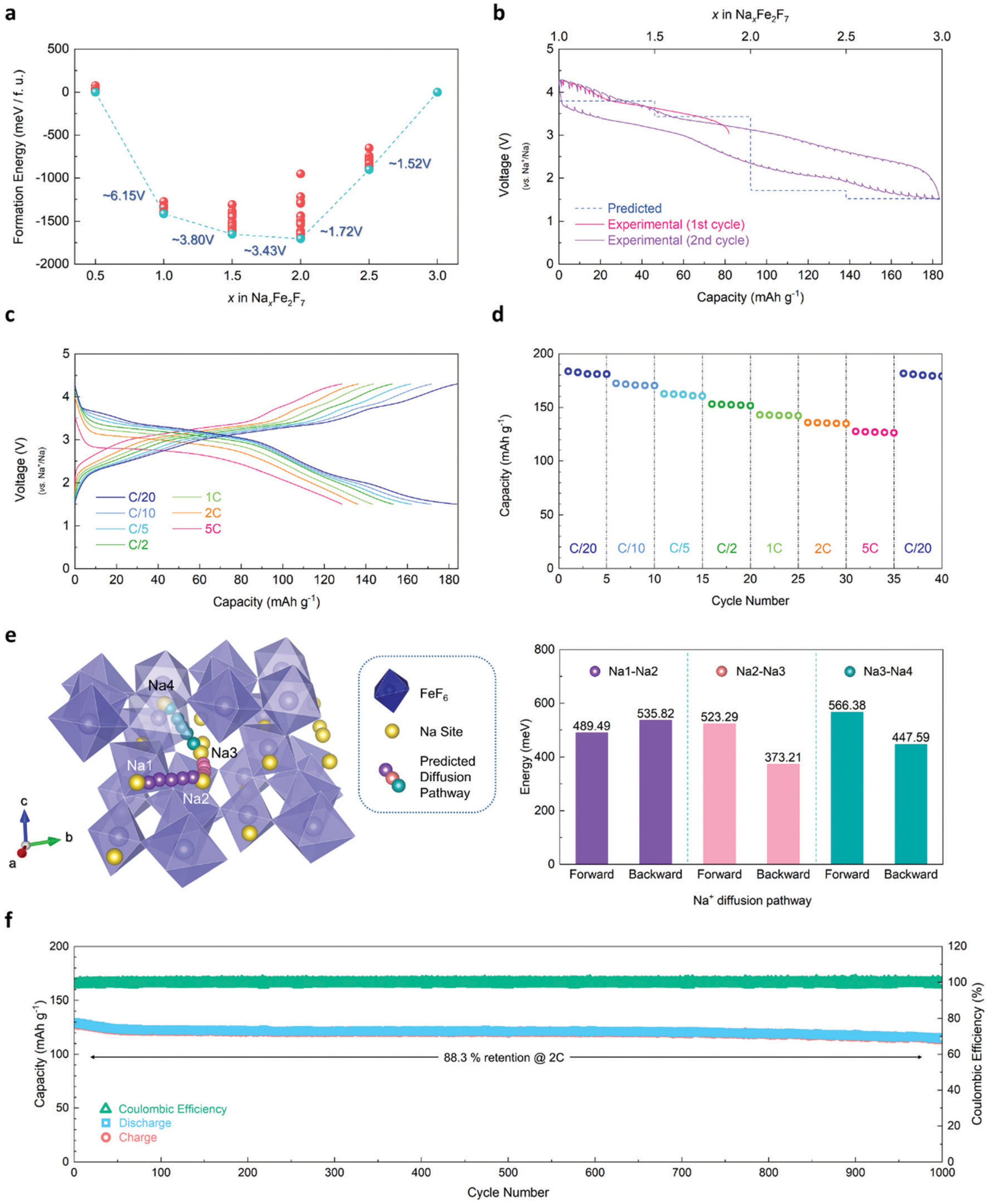

Fig. 3 (a) Formation energy with derived theoretical voltage of T-$Na_xFe_2F_7$ ($0.5 \leq x \leq 3$). (b) Comparison of theoretical voltage prediction and GITT spectra for T-$Na_xFe_2F_7$ ($1 \leq x \leq 3$). (c) Charge/discharge curves of T-$Na_2Fe_2F_7$ in the range of 1.5–4.3 V at various discharge current rates and a charge current rate of C/20. (d) Power-capability of T-$Na_2Fe_2F_7$. (e) Three-dimensional Na^+ diffusion pathways with energy landscape determined using the NEB method in the T-$Na_xFe_2F_7$ structure. (f) Cycling performance of T-$Na_2Fe_2F_7$ over 1000 cycles at 2C.

specific capacity of T-$Na_xFe_2F_7$ was retained up to ~129 mA h g^{-1}, corresponding to ~70% of its theoretical capacity. Moreover, we predicted the theoretical activation barrier energies for the Na^+ diffusion pathways in T-$Na_xFe_2F_7$ using the nudged elastic band (NEB) method based on first-principles calculations (Fig. 3e). The activation barrier energies were considered sufficiently low for facile Na^+ migration along three-dimensional pathways in the structure. These findings indicate the suitable power-capability of T-$Na_xFe_2F_7$ in Na cells. In particular, we verified the ultra-long cycling performance with more than ~88% capacity retention for 1000 cycles at 2C (Fig. 3f). The applicability of $Na_2Fe_2F_7$ was further examined by pairing with a hard-carbon anode. Before the full-cell assembly, pre-treatment of both electrodes was performed, including pre-cycling of the hard carbon anode between 0.01 and 2 V (*vs.* Na^+/Na) to eliminate the irreversible initial capacity and full discharge of the T-$Na_xFe_2F_7$ cathode to 1.5 V (*vs.* Na^+/Na). The full cell delivered an initial specific capacity of 118 mA h g^{-1}, with a capacity retention of over 88% for 1000 cycles at a current density of 368 mA g^{-1} (Fig. S7, ESI†). In addition, T-$Na_2Fe_2F_7$ without pre-sodiation just exhibits reversible 1 mol Na^+ de/intercalation at a T-$Na_2Fe_2F_7$//hard carbon full-cell system, which indicates that the full-cell capacity is cut in approximately half compared to a pre-sodiated T-$Na_3Fe_2F_7$//hard carbon full-cell system (Fig. S8, ESI†). Notably, T-$Na_xFe_2F_7$ was able to retain its original morphology and crystal structure for 1000 cycles (Fig. S9 and S10, ESI†). The electrochemical performance of T-$Na_xFe_2F_7$ was more prominent compared with that of other cathode materials for NIBs with high-voltage and high-capacity characteristics such as layered-type oxides, polyanions and Prussian-blue (Fig. 4 and Table S3 (ESI†)), including a large energy density of ~400 W h kg^{-1} at a power density of 2852 W kg^{-1} and ~88% capacity retention after 1000 cycles.[36–45] Besides, to identify the interface product after a long-term cycle, we performed X-ray photoelectron spectroscopy (XPS) analyses on 1-cycled and 1000-cycled T-$Na_2Fe_2F_7$ electrodes and compared them. As presented in Fig. S11 (ESI†), it was verified that the cathode–electrolyte interface (CEI) of T-$Na_2Fe_2F_7$ electrodes is well retained even after 1000 cycles without severe change, which is also considered as one of the reasons for the highly stable cycling performance of T-$Na_2Fe_2F_7$ electrodes under the NIB system.

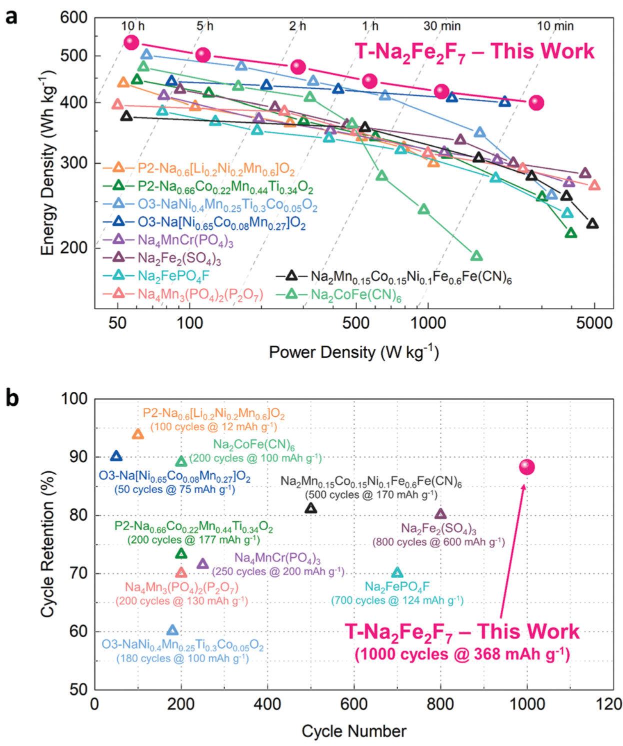

Fig. 4 (a) Ragone plot of T-$Na_2Fe_2F_7$ and other cathode materials for NIBs. (b) Comparison of the cycling performance of T-$Na_2Fe_2F_7$ and other cathode materials for NIBs.

In addition, we compared the XRD patterns of hard carbon electrodes before and after cycling for 1000 cycles. As presented in Fig. S12 (ESI†), it is difficult to detect considerable change of XRD patterns after 1000 cycles, because the pristine hard carbon electrode exhibits originally the low crystalline phase. However, it was observed that the (200) XRD peak at the 1000-cycled hard carbon electrode becomes more broad with lowered intensity compared to that at the pristine hard carbon, which indicates that structural degradation occurred at the hard carbon during repeated 1000 cycles. Moreover, SEM analyses revealed that numerous cracks are generated on the surface of the hard carbon electrode surface after 1000 cycles, whereas the surface of the T-$Na_2Fe_2F_7$ electrode is stably retained under the same conditions (Fig. S13, ESI†). Furthermore, we prepared cross-SEM analyses for the T-$Na_2Fe_2F_7$ electrode before and after cycling for 1000 cycles. As shown in Fig. S14 (ESI†), the T-$Na_2Fe_2F_7$ electrode is stably maintained on the aluminum foil even after 1000 cycles, without severe cracking, volume expansion or electrode exfoliation. These results indicate that hard carbon experiences large volume change during repeated charge/discharge compared to T-$Na_2Fe_2F_7$. Thus, we confirmed that the failure mechanism for the T-$Na_xFe_2F_7$// hard carbon full cell is determined by not T-$Na_xFe_2F_7$ but hard carbon.

Reaction mechanism of T-$Na_2Fe_2F_7$ during Na^+ de/intercalation

We speculated that the exceptional excellent cyclability of T-$Na_xFe_2F_7$ could likely be attributed to the simple and small structural change resulting from the strong bonds in the FeF_6 octahedra during Na^+ de/intercalation. To obtain insight into the structural change during charge/discharge, the T-$Na_xFe_2F_7$ electrode was investigated using *operando* synchrotron XRD (*o*-SXRD) (Fig. 5a). In addition, Fig. S15 (ESI†) shows the full *operando* synchrotron XRD patterns of T-$Na_xFe_2F_7$. Overall, the XRD peaks of T-$Na_xFe_2F_7$ monotonously shifted during charge/discharge, although the amplitude was very small in 2θ. The relative intensities of the XRD peaks, such as the (003) and (202) peaks, gradually varied during charge/discharge because of reversible Na^+ de/intercalation (Fig. 5b). Through Rietveld refinement analyses, we verified that despite the large size of Na^+, the total volume difference between the fully charged T-$Na_1Fe_2F_7$ and fully discharged T-$Na_3Fe_2F_7$ was less than 1% (Fig. 5c and d), which is significantly less than the volume change observed in not only layered-type cathode materials but also various polyanionic cathode materials for NIBs during charge/discharge (Fig. S16, ESI†).[21,46–50] Moreover, we performed *ex situ* XRD analyses of T-$Na_xFe_2F_7$ electrodes with various Na contents (Fig. S17, ESI†). Continuous shift of the XRD peaks was observed during Na^+ de/intercalation at the T-$Na_xFe_2F_7$ structure. Through Rietveld refinement, we calculated the lattice parameters and volume of the various T-$Na_xFe_2F_7$ electrodes, which indicates that the total volume difference between T-$Na_1Fe_2F_7$ and T-$Na_3Fe_2F_7$ was just ~0.97% (Fig. S18, ESI†). These *ex situ* XRD results are well matched with the *operando* synchrotron XRD results. We speculate that the negligible volume change of T-$Na_xFe_2F_7$ during charge/discharge

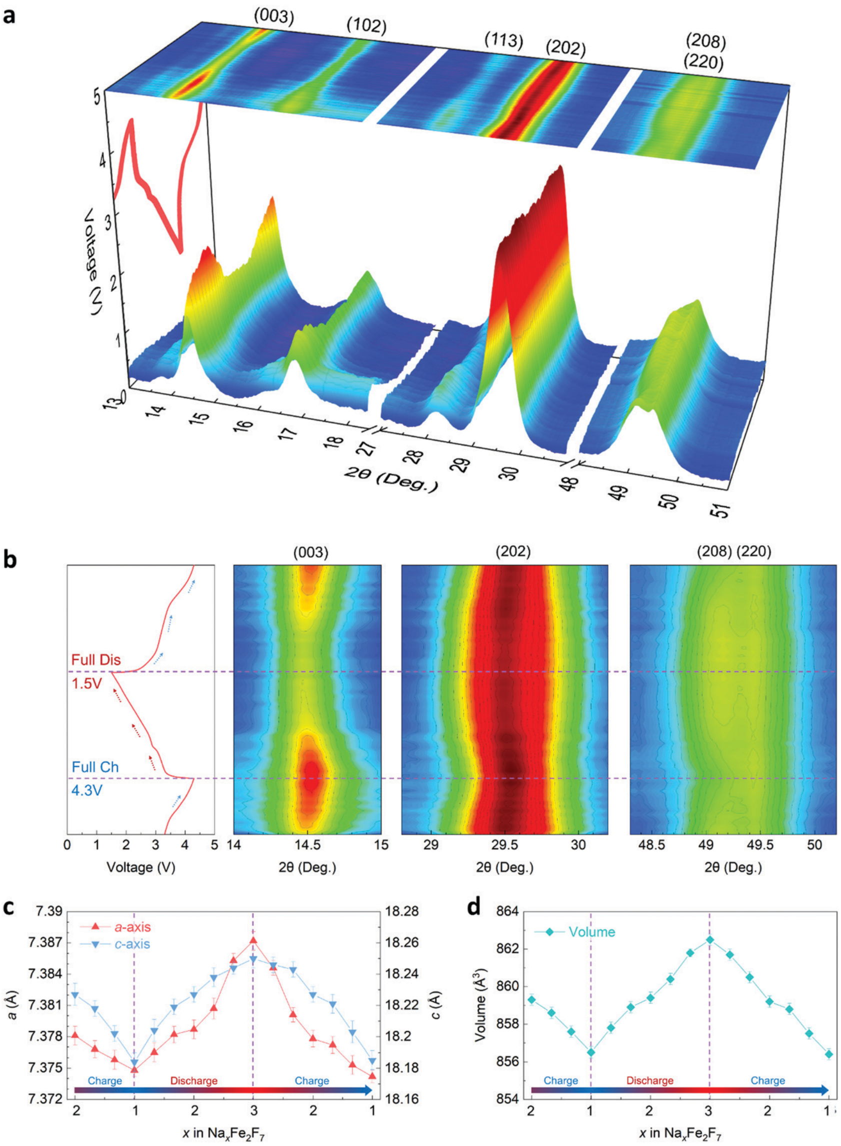

Fig. 5 (a) *o*-SXRD patterns of T-Na$_x$Fe$_2$F$_7$ ($1 \leq x \leq 3$) during charge/discharge. (b) Magnified view of *o*-SXRD patterns with charge/discharge curves of T-Na$_x$Fe$_2$F$_7$ ($1 \leq x \leq 3$). (c and d) Change in (c) lattice parameter and (d) volume as a function of Na content in T-Na$_x$Fe$_2$F$_7$ ($1 \leq x \leq 3$) verified through Rietveld refinement.

results can be attributed to (1) the well-retained trigonal-based crystal structure without any phase transition during Na$^+$ de/intercalation unlike in layered-type cathode materials for NIBs and (2) the crystal structure of T-Na$_x$Fe$_2$F$_7$ based on corner-shared FeF$_6$ octahedra providing more freedom for rotation of the octahedra, allowing suppression of severe volume expansion/shrinkage during Na$^+$ de/intercalation, unlike in layered-type cathode materials based on edge-shared MO$_6$ octahedra.

Moreover, we observed that the broadness of the XRD peaks reversibly increased and decreased with variation of the residual strain as a function of Na content in the structure, which is another reason for Na$^+$ de/intercalation in T-Na$_x$Fe$_2$F$_7$ during charge/discharge. The lattice strain was calculated using the Williamson–Hall isotropic strain model (W–H ISM).[51,52] Before estimating the lattice strain, the full width at half maximum (FWHM) corrected for peak broadening due to the instrumental effect was calculated using the following equation:

$$\beta_{hkl} = \sqrt{\beta_o^2 - \beta_i^2},$$

where β_{hkl} is the corrected FWHM, β_o is the observed FWHM, and β_i is the instrumental broadening, which was collected from lanthanum hexaboride (LaB$_6$) standard powder.[53] The corrected FWHM is represented by the contribution of lattice strain and crystallite size in the W–H ISM. The two independent factors, lattice strain and crystallite size, also contributed to the total peak broadening, as expressed in the following equation:

$$\beta_{hkl} \cos\theta_{hkl} = \frac{K\lambda}{D} + 4\varepsilon \sin\theta_{hkl},$$

where θ_{hkl} is the Bragg angle, K is the shape factor (=0.9), λ is the X-ray wavelength, and ε is the lattice strain. Using the equation mentioned above, this information can be expressed in the form of a linear fitting plot with an x-axis of $4\sin\theta_{hkl}$ and y-axis of $\beta_{hkl}\cos\theta_{hkl}$ (Fig. S19, ESI†). As shown in Table S4 (ESI†), it is reasonable that the lattice strain of $Na_xFe_2Fe_7$ gradually increases (or decreases) with Na^+ intercalation (or deintercalation). The total lattice-strain change of $Na_xFe_2Fe_7$ during charge/discharge based on the o-SXRD patterns is ~0.249%, in good agreement with the small volume change of $Na_xFe_2Fe_7$ during Na^+ de/intercalation. Moreover, based on the *ex situ* XRD patterns of T-$Na_xFe_2F_7$, we performed Williamson–Hall isotropic strain analyses carefully. As presented in Fig. S20 and Table S5 (ESI†) below, it was verified that the total lattice-strain change of $Na_xFe_2Fe_7$ during charge/discharge, based on the *ex situ* XRD data, was just ~0.254%, which is consistent with o-SXRD result. This result on the variation of the lattice strain also indicates the reversible Na^+ de/intercalation in the T-$Na_xFe_2Fe_7$ structure during charge/discharge.

Further analyses using TEM clearly confirmed that T-$Na_xFe_2F_7$ undergoes small structural change despite 2 mol Na^+ de/intercalation. Fig. 6 shows only small differences in the SAED patterns of the as-prepared, fully charged, and fully discharged samples; the SAED patterns of the three samples were also consistent with the simulated pattern of T-$Na_2Fe_2F_7$ along the $[\bar{2}\bar{1}1]$ zone axis. The d-spacing of the (011) plane of the T-$Na_2Fe_2F_7$ phase was observed to slightly increase (or decrease) during discharge (or charge) (Fig. S21, ESI†), which is consistent with the o-SXRD results. In addition, we performed TEM-based electron energy loss spectroscopy (TEM-EELS) analyses on the three samples. It was revealed that the reversible Fe^{2+}/Fe^{3+} redox reaction of T-$Na_xFe_2F_7$ occurred during charge/discharge (Fig. 7a), which also indicates the good preparation of the as-prepared, fully charged, and fully discharged samples with different Na contents.[54] Moreover, *ex situ* XANES analyses confirmed that the Fe K-edge of T-$Na_xFe_2F_7$ shifted toward lower (higher) energy levels during discharge (charge) (Fig. 7b). These results indicate the reversible Fe^{2+}/Fe^{3+} redox reaction arising from 1 mol Na^+ deintercalation from the T-$Na_2Fe_2F_7$ structure as well as additional 1 mol Na^+ intercalation in the structure (a total of 2 mol Na^+ de/intercalation at T-$Na_xFe_2F_7$). These *ex situ* TEM-EELS and XANES results were also confirmed by first-principles calculations. Fig. 7c shows that the total integrated spin number on Fe ions in T-$Na_1Fe_2F_7$ and T-$Na_3Fe_2F_7$ was five and four, respectively, indicating the occurrence of Fe^{2+}/Fe^{3+} redox reaction at T-$Na_xFe_2F_7$ during charge/discharge. In addition, because of the weaker bond between Fe^{2+} and F^- than between Fe^{3+} and F^-, the Fe^{2+}/Fe^{3+} redox reaction affects the local structural change of Fe–F bonding in the T-$Na_xFe_2F_7$ structure. *Ex situ* extended X-ray absorption fine structure (EXAFS) analyses revealed that the Fe–F bond distance slightly increased with reduction from Fe^{3+} to Fe^{2+} during Na^+ intercalation (Fig. 7d), as verified through first-principles calculations (Fig. 7e). Moreover, we conducted the EXAFS fitting for T-$Na_xFe_2F_7$ ($1 \le x \le 3$) (Fig. S22 and Table S6, ESI†). The fitting process was performed under k^2-weight conditions in the fitting range of 1.0–2.2 Å for the first shell, corresponding to the Fe–F bond. The amplitude reduction factor, $S_0{}^2$, was set to 1.0. As a result, the average Fe–F bonding distance increased from 1.925 Å to 2.127 Å with Na^+ intercalation into T-$Na_xFe_2F_7$, which was consistent with the first-principles calculations results. Based on the various experimental and computational results, we confirmed that the small structural change during charge/discharge is the driving force that enables the ultra-long cycling performance of T-$Na_xFe_2F_7$ as a promising cathode for NIBs.

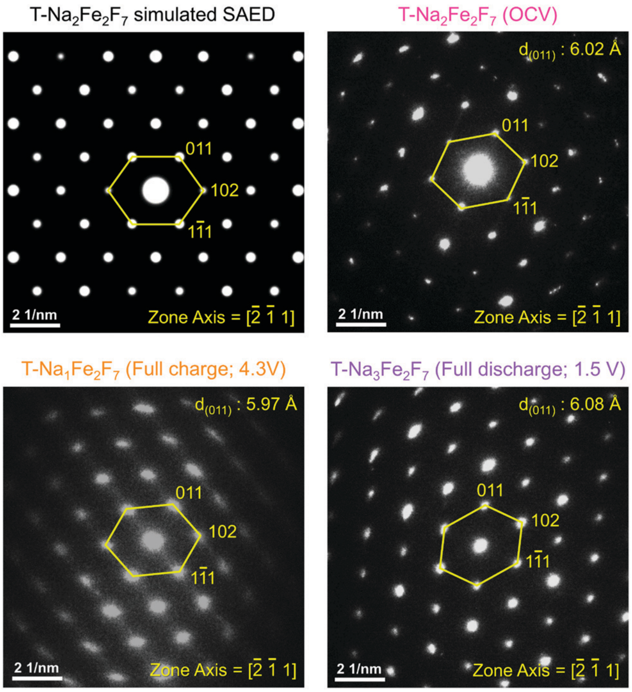

Fig. 6 SAED pattern of T-$Na_xFe_2F_7$ ($1 \le x \le 3$).

Conclusions

In this work, we investigated the use of earth-abundant elements such as Na, Fe, and F in promising cathodes for NIBs. The structural stabilization toward a T-$Na_2Fe_2F_7$ three-dimensional framework resulted in facile Na^+ de/interaction into/out of the generated large three-dimensional Na^+ diffusion pathway *via* a solid-solution reaction from $Na_1Fe^{(3+)}{}_2F_7$ to $Na_3Na^{(2+)}{}_2F_7$ as well as high structural stability, preventing considerable structural change during charge/discharge. The movement of 2 mol Na^+ per formula unit corresponds to the theoretical capacity (184 mA h g^{-1}), which is the highest value ever achieved for three-dimensional structured compounds. Furthermore, the interaction of the inductive effect with the highest electronegativity of F ions is a plausible explanation for the acceptable average operation voltage of ~3.1 V (*vs.* Na^+/Na) despite the Fe^{2+}/Fe^{3+} redox reaction. The outstanding power-capability is attributed to the low activation barrier energy for facile Na^+ diffusion in the structure, which enables high capacity delivered at 5C that reaches ~70% of the theoretical capacity. The long-term structural stability was further confirmed

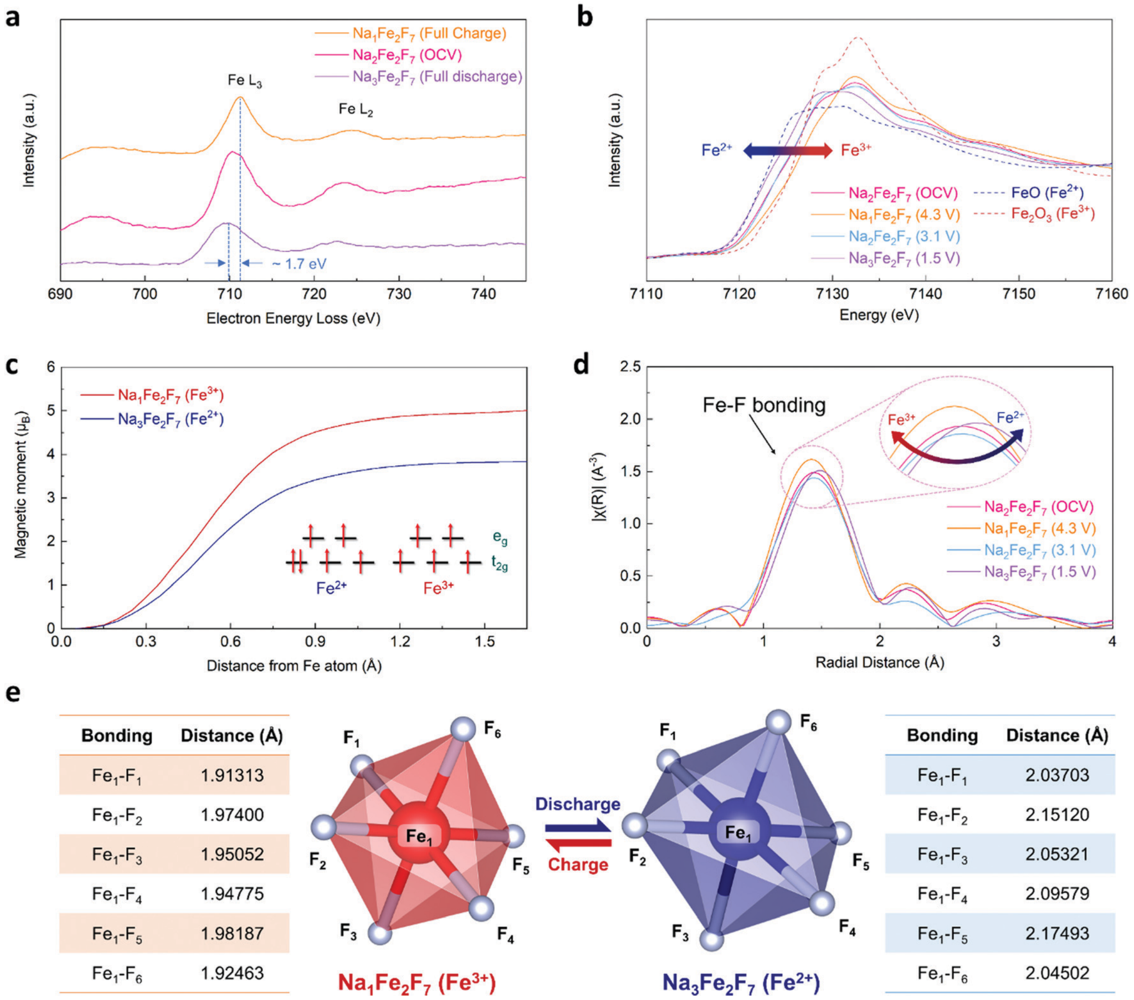

Bonding	Distance (Å)
Fe$_1$-F$_1$	1.91313
Fe$_1$-F$_2$	1.97400
Fe$_1$-F$_3$	1.95052
Fe$_1$-F$_4$	1.94775
Fe$_1$-F$_5$	1.98187
Fe$_1$-F$_6$	1.92463

Bonding	Distance (Å)
Fe$_1$-F$_1$	2.03703
Fe$_1$-F$_2$	2.15120
Fe$_1$-F$_3$	2.05321
Fe$_1$-F$_4$	2.09579
Fe$_1$-F$_5$	2.17493
Fe$_1$-F$_6$	2.04502

Fig. 7 (a) TEM-EELS spectra of T-Na$_x$Fe$_2$F$_7$ ($1 \leq x \leq 3$). (b) K-edge XANES spectra of T-Na$_x$Fe$_2$F$_7$ ($1 \leq x \leq 3$). (c) Integrated spin moments of T-Na$_1$Fe$_2$F$_7$ and T-Na$_3$Fe$_2$F$_7$. (d) EXAFS spectra of T-Na$_x$Fe$_2$F$_7$ ($1 \leq x \leq 3$). (e) Fe–F bonding distances of FeF$_6$ in T-Na$_1$Fe$_2$F$_7$ and T-Na$_3$Fe$_2$F$_7$ structures verified through first-principles calculations.

at 2C, namely, ∼88% capacity retention for 1000 cycles. Despite the outstanding electrochemical performances such as stable cycling performance and large specific capacity, the following issues should be solved for applications of T-Na$_2$Fe$_2$F$_7$ as the cathode for commercialized NIBs; (1) a pre-sodiation process by Na-deficient phase, (2) a nanosizing process by low electronic conductivity and (3) low density by nanosized particles. Thus, follow-up studies will be focused on in the future, such as addition of Na-ion sacrificial salt to the cathode for compensation of deficient Na ions and homogenous particle coating of conductive materials for enhancing electronic conductivity without nanosizing. We expect that our work will introduce a milestone for the discovery of new low-cost cathode materials with high power-capability and long-term cyclability for not only NIBs but also other types of rechargeable batteries. In addition, the usage of earth-abundant Na and Fe element implies the potentially low production cost. If the comparison standard for determining the production cost is just metal price, T-Na$_2$Fe$_2$F$_7$ has a great merit compared to other well-known cathode materials for NIBs such as Na$_x$Cu$_{1-y-z}$Fe$_y$Mn$_z$O$_2$,[55–58] because of lower price of Fe than those of other metals such as Cu and Mn. Moreover, more outstanding cyclability of T-Na$_2$Fe$_2$F$_7$ than oxide-based cathode materials for NIBs can result in a decreased number of times for replacing batteries, which is also one of the high cost-competitive points of T-Na$_2$Fe$_2$F$_7$. Whereas degrees of freedom in precursor selection are high for perpetration of other oxide-based cathode materials, fluoride-based precursors should be used for preparation of T-Na$_2$Fe$_2$F$_7$. Thus, we guess mass-production of fluoride-based precursors is very important to prepare T-Na$_2$Fe$_2$F$_7$ at a low price industrially.

Author contributions

H. P. and Y. L. designed/performed the combined studies of various experiments and first-principles calculations, and wrote the manuscript. M.-K. C. carried out the HR-TEM measurement with EELS analyses. J. Kang assisted the XAS measurements. W. K., Y. H. J. and T.-Y. J. contributed to the *operando* synchrotron XRD measurements. J. H. and H. K. provided constructive advice for the experimental design and analyses. S.-T. M. contributed to reviewing and editing the manuscript. J. Kim conceived the original idea, supervised the research, and contributed to the writing of the manuscript.

Conflicts of interest

There are no conflicts to declare.

Acknowledgements

This work was supported by the National Research Foundation of Korea funded by the Ministry of Science and ICT of Korea (NRF-2018K1A4A3A01064272, NRF-2019M3D1A2104105, NRF-2020M2D8A2070870, and NRF-2020M3H4A1A03084256). Also, this work was supported by the institutional program of the Korea Institute of Science and Technology (KIST, Project No. 2V08350).

References

1 K. Kang, Y. S. Meng, J. Bréger, C. P. Grey and G. Ceder, *Science*, 2006, **311**, 977–980.

2 J.-M. Tarascon and M. Armand, *Mater. Sustainable Energy*, 2010, **26**, 171–179.

3 B. Dunn, H. Kamath and J.-M. Tarascon, *Science*, 2011, **334**, 928–935.

4 D. Eum, B. Kim, S. J. Kim, H. Park, J. Wu, S.-P. Cho, G. Yoon, M. H. Lee, S.-K. Jung, W. Yang, W. M. Seong, K. Ku, O. Tamwattana, S. K. Park, I. Hwang and K. Kang, *Nat. Mater.*, 2020, **19**, 419–427.

5 B. J. Hwang, Y. W. Tsai, D. Carlier and G. Ceder, *Chem. Mater.*, 2003, **15**, 3676–3682.

6 N. Yabuuchi, M. Kajiyama, J. Iwatate, H. Nishikawa, S. Hitomi, R. Okuyama, R. Usui, Y. Yamada and S. Komaba, *Nat. Mater.*, 2012, **11**, 512–517.

7 M. Bianchini, J. Wang, R. Clément and G. Ceder, *Adv. Energy Mater.*, 2018, **8**, 1801446.

8 J. Vergnet, M. Saubanère, M. L. Doublet and J. M. Tarascon, *Joule*, 2020, **4**, 420–434.

9 M. Bianchini, P. Xiao, Y. Wang and G. Ceder, *Adv. Energy Mater.*, 2017, **7**, 1700514.

10 H. Kim, Y. Ishado, Y. Tian and G. Ceder, *Adv. Funct. Mater.*, 2019, **29**, 1902392.

11 Y. Kawabe, N. Yabuuchi, M. Kajiyama, N. Fukuhara, T. Inamasu, R. Okuyama, I. Nakai and S. Komaba, *Electrochem. Commun.*, 2011, **13**, 1225–1228.

12 Y. Lu, L. Wang, J. Cheng and J. B. Goodenough, *Chem. Commun.*, 2012, **48**, 6544.

13 A. J. Fernández-Ropero, M. J. Piernas-Muñoz, E. Castillo-Martínez, T. Rojo and M. Casas-Cabanas, *Electrochim. Acta*, 2016, **210**, 352–357.

14 M. Tang, Y. Wu, Y. Chen, C. Jiang, S. Zhu, S. Zhuo and C. Wang, *J. Mater. Chem. A*, 2019, **7**, 486–492.

15 H. Kim, J. E. Kwon, B. Lee, J. Hong, M. Lee, S. Y. Park and K. Kang, *Chem. Mater.*, 2015, **27**, 7258–7264.

16 M. Chen, Q. Liu, S. Wang, E. Wang, X. Guo and S. Chou, *Adv. Energy Mater.*, 2019, **9**, 1803609.

17 J. Y. Hwang, S. T. Myung and Y. K. Sun, *Chem. Soc. Rev.*, 2017, **46**, 3529–3614.

18 S. Kikkawa, S. Miyazaki and M. Koizumi, *Mater. Res. Bull.*, 1985, **20**, 373–377.

19 N. Yabuuchi, H. Yoshida and S. Komaba, *Electrochemistry*, 2012, **80**, 716–719.

20 N. Ortiz-Vitoriano, N. E. Drewett, E. Gonzalo and T. Rojo, *Energy Environ. Sci.*, 2017, **10**, 1051–1074.

21 R. Tripathi, S. M. Wood, M. S. Islam and L. F. Nazar, *Energy Environ. Sci.*, 2013, **6**, 2257.

22 N. Recham, J.-N. Chotard, L. Dupont, K. Djellab, M. Armand and J.-M. Tarascon, *J. Electrochem. Soc.*, 2009, **156**, A993.

23 P. Barpanda, J.-N. Chotard, N. Recham, C. Delacourt, M. Ati, L. Dupont, M. Armand and J.-M. Tarascon, *Inorg. Chem.*, 2010, **49**, 7401–7413.

24 A. Plewa, A. Kulka, E. Hanc, W. Zając, J. Sun, L. Lu and J. Molenda, *J. Mater. Chem. A*, 2020, **8**, 2728–2740.

25 H. Park, H. Kim, W. Ko, J. H. Jo, Y. Lee, J. Kang, I. Park, S.-T. Myung and J. Kim, *Energy Storage Mater.*, 2020, **28**, 47–54.

26 J. Kang, H. Park, H. Kim, J. H. Jo, W. Ko, Y. Lee, S. Myung and J. Kim, *ACS Sustainable Chem. Eng.*, 2020, **8**, 163–171.

27 J. Lu, S. Nishimura and A. Yamada, *Electrochem. Commun.*, 2017, **79**, 51–54.

28 Y.-U. Park, D.-H. Seo, H.-S. Kwon, B. Kim, J. Kim, H. Kim, I. Kim, H.-I. Yoo and K. Kang, *J. Am. Chem. Soc.*, 2013, **135**, 13870–13878.

29 I. D. Brown and D. Altermatt, *Acta Crystallogr., Sect. B: Struct. Sci.*, 1985, **41**, 244–247.

30 P.-F. Wang, Y. You, Y.-X. Yin and Y.-G. Guo, *Adv. Energy Mater.*, 2018, **8**, 1701912.

31 Y. Huang, Y. Zheng, X. Li, F. Adams, W. Luo, Y. Huang and L. Hu, *ACS Energy Lett.*, 2018, **3**, 1604–1612.

32 J. H. Jo, J.-Y. Hwang, J. Choi, Y.-K. Sun and S.-T. Myung, *ACS Appl. Mater. Interfaces*, 2019, **11**, 43312–43319.

33 R. Chen, P. Zavalij and M. S. Whittingham, *Chem. Mater.*, 1996, **8**, 1275–1280.

34 A. Van der Ven, J. C. Thomas, Q. Xu and J. Bhattacharya, *Math. Comput. Simul.*, 2010, **80**, 1393–1410.

35 J. Kim, H. Kim, I. Park, Y. U. Park, J. K. Yoo, K. Y. Park, S. Lee and K. Kang, *Energy Environ. Sci.*, 2013, **6**, 830–834.

36 E. De La Llave, P. K. Nayak, E. Levi, T. R. Penki, S. Bublil, P. Hartmann, F. F. Chesneau, M. Greenstein, L. F. Nazar and D. Aurbach, *J. Mater. Chem. A*, 2017, **5**, 5858–5864.

37 Q.-C. Wang, E. Hu, Y. Pan, N. Xiao, F. Hong, Z.-W. Fu, X.-J. Wu, S.-M. Bak, X.-Q. Yang and Y.-N. Zhou, *Adv. Sci.*, 2017, **4**, 1700219.

38 C. Zhou, L. Yang, C. Zhou, B. Lu, J. Liu, L. Ouyang, R. Hu, J. Liu and M. Zhu, *ACS Appl. Mater. Interfaces*, 2019, **11**, 7906–7913.

39 H.-H. Sun, J.-Y. Hwang, C. S. Yoon, A. Heller and C. B. Mullins, *ACS Nano*, 2018, **12**, 12912–12922.

40 W. Zhang, H. Li, Z. Zhang, M. Xu, Y. Lai and S. Chou, *Small*, 2020, **16**, 2001524.

41 M. Chen, D. Cortie, Z. Hu, H. Jin, S. Wang, Q. Gu, W. Hua, E. Wang, W. Lai, L. Chen, S.-L. Chou, X.-L. Wang and S.-X. Dou, *Adv. Energy Mater.*, 2018, **8**, 1800944.

42 W. Ko, J.-K. Yoo, H. Park, Y. Lee, H. Kim, Y. Oh, S.-T. Myung and J. Kim, *J. Power Sources*, 2019, **432**, 1–7.

43 H. Kim, G. Yoon, I. Park, K.-Y. Park, B. Lee, J. Kim, Y.-U. Park, S.-K. Jung, H.-D. Lim, D. Ahn, S. Lee and K. Kang, *Energy Environ. Sci.*, 2015, **8**, 3325–3335.

44 B. Xie, P. Zuo, L. Wang, J. Wang, H. Huo, M. He, J. Shu, H. Li, S. Lou and G. Yin, *Nano Energy*, 2019, **61**, 201–210.

45 X. Wu, C. Wu, C. Wei, L. Hu, J. Qian, Y. Cao, X. Ai, J. Wang and H. Yang, *ACS Appl. Mater. Interfaces*, 2016, **8**, 5393–5399.

46 K. T. Lee, T. N. Ramesh, F. Nan, G. Botton and L. F. Nazar, *Chem. Mater.*, 2011, **23**, 3593–3600.

47 M. Galceran, D. Saurel, B. Acebedo, V. V. Roddatis, E. Martin, T. Rojo and M. Casas-Cabanas, *Phys. Chem. Chem. Phys.*, 2014, **16**, 8837–8842.

48 Z. Jian, W. Han, X. Lu, H. Yang, Y.-S. Hu, J. Zhou, Z. Zhou, J. Li, W. Chen, D. Chen and L. Chen, *Adv. Energy Mater.*, 2013, **3**, 156–160.

49 H. Gao, I. D. Seymour, S. Xin, L. Xue, G. Henkelman and J. B. Goodenough, *J. Am. Chem. Soc.*, 2018, **140**, 18192–18199.

50 M. Chen, L. Chen, Z. Hu, Q. Liu, B. Zhang, Y. Hu, Q. Gu, J.-L. Wang, L.-Z. Wang, X. Guo, S.-L. Chou and S.-X. Dou, *Adv. Mater.*, 2017, **29**, 1605535.

51 P. Muhammed Shafi and A. Chandra Bose, *AIP Adv.*, 2015, **5**, 057137.

52 K. Venkateswarlu, A. Chandra Bose and N. Rameshbabu, *Phys. B*, 2010, **405**, 4256–4261.

53 B. B. He, *Two-dimensional X-ray Diffraction*, John Wiley & Sons, Inc., Hoboken, NJ, USA, 2018.

54 D. K. Mann, J. Xu, N. E. Mordvinova, V. Yannello, Y. Ziouani, N. González-Ballesteros, J. P. S. Sousa, O. I. Lebedev, Y. V. Kolen'ko and M. Shatruk, *Chem. Sci.*, 2019, **10**, 2796–2804.

55 J. Xu, J. Chen, K. Zhang, N. Li, L. Tao and C.-P. Wong, *Nano Energy*, 2020, **78**, 105142.

56 Y. Li, Z. Yang, S. Xu, L. Mu, L. Gu, Y. S. Hu, H. Li and L. Chen, *Adv. Sci.*, 2015, **2**, 1–7.

57 E. Talaie, S. Y. Kim, N. Chen and L. F. Nazar, *Chem. Mater.*, 2017, **29**, 6684–6697.

58 H. Fu, G. Fan, J. Zhou, X. Yu, X. Xie, J. Wang, B. Lu and S. Liang, *Inorg. Chem.*, 2020, **59**, 13792–13800.